nature neuroscience

TECHNICAL REPORT

https://doi.org/10.1038/s41593-018-0211-4

In vivo measurement of afferent activity with axon-specific calcium imaging

Gerard Joey Broussard[1], Yajie Liang[2], Marina Fridman[3], Elizabeth K. Unger[1], Guanghan Meng[2,4], Xian Xiao[1,5], Na Ji[2,4], Leopoldo Petreanu[3*] and Lin Tian[1*]

In vivo calcium imaging from axons provides direct interrogation of afferent neural activity, informing the neural representations that a local circuit receives. Unlike in somata and dendrites, axonal recording of neural activity—both electrically and optically—has been difficult to achieve, thus preventing comprehensive understanding of neuronal circuit function. Here we developed an active transportation strategy to enrich GCaMP6, a genetically encoded calcium indicator, uniformly in axons with sufficient brightness, signal-to-noise ratio, and photostability to allow robust, structure-specific imaging of presynaptic activity in awake mice. Axon-targeted GCaMP6 enables frame-to-frame correlation for motion correction in axons and permits subcellular-resolution recording of axonal activity in previously inaccessible deep-brain areas. We used axon-targeted GCaMP6 to record layer-specific local afferents without contamination from somata or from intermingled dendrites in the cortex. We expect that axon-targeted GCaMP6 will facilitate new applications in investigating afferent signals relayed by genetically defined neuronal populations within and across specific brain regions.

Neural circuits consist of large populations of cell bodies connected by axons and dendrites. Understanding circuit computations (and even the computations of single neurons) requires knowing the neural representation carried by inputs, local neurons, and outputs that lead to input–output transformations. Axons are very thin (typically less than 1 μm in diameter), branch numerous times, can vary in length, and travel the full extent of the brain, thus making activity-recording difficult. Microelectrode-based recording methods do not allow isolation of single axons and lack the genetic specificity required to identify the source of the recorded input signals. Genetically encoded calcium indicators (GECIs; for review, see ref. [1]), such as the GCaMP family[2–5], have enabled recordings from the somata and dendrites of genetically defined neuronal populations in behaving animals. However, optical recording from individual axons and presynaptic structures with GECIs is suboptimal, thus limiting comprehensive interrogation of afferent inputs.

Untargeted GCaMPs (u-GCaMPs) preferentially label somatodendritic compartments and diffuse poorly to distal axons. Low expression levels of GECIs in presynaptic structures make even visualizing axons with expression difficult, and functional imaging of dimly labeled axons produces poor signal-to-noise ratios (SNRs), particularly deep in tissue where light scattering requires a high photon budget. Consequently, axonal GECI imaging is typically performed only under near-ideal conditions, such as shallow terminal fields of relatively short projections[6–14]. Even so, low SNR and contamination from intermingled dendritic arbors closer to the expression source degrade imaging quality and complicate assignment of fluorescence to specific axons due to overlapping dendritic signals. Presynaptically targeted GCaMPs have been developed[15], but suffer substantially from photobleaching[16]. We thus developed an approach for axonal GCaMP imaging that offers greater enrichment and photostability than previous techniques.

Results

Engineering and characterization of an axon-enriched GCaMP. To design a high-efficacy axon-enriched GCaMP6, we screened a panel of targeting motifs that have been previously reported to drive axonal localization (Supplementary Fig. 1a). We chose eight motifs with diverse targeting mechanisms and fused them to either the N or C terminus of GCaMP6m. These motifs included the 20 residue dipalmitoylation domain found at the N terminus of growth-associated protein-43 (GAP43)[17], the 15-residue C terminus of the amyloid precursor protein[18], the ankyrin-B binding motif derived from the N and P/Q-type voltage-dependent calcium channels[19], the mRNA localization zip code found within the 3′ untranslated region of the tau gene[20], the 26-residue tandem palmitoylation and myristoylation domains found at the N terminus of the Src tyrosine kinase Lck[21,22], the synthetic myosin VI binding domain derived from peptides found in Optineurin and in Disabled homolog 2[23], the 20-residue palmitoylation domain found at the C terminus of Paralemmin[24], and finally the full-length Synaptophysin, which was previously reported to target GCaMP effectively to axons[15] but also rapidly photobleaches during in vivo imaging[16] (Fig. 1a and Supplementary Fig. 1a).

We first characterized the expression pattern of each construct in dissociated rat hippocampal neuronal culture. We measured a normalized axon-to-dendrite ratio (nADR)[25] to determine the extent to which each probe localized to axonal and somatodendritic compartments relative to a co-expressed, untargeted red fluorophore (mRuby2; Fig. 1b,c and Supplementary Fig. 1b). The 20-residue dipalmitoylation domain derived from the N terminus of GAP43 drove the highest enrichment of GCaMP6m in axons (Fig. 1b and Supplementary Fig. 1b), with ~fivefold increased nADR compared to u-GCaMP6m (nADR of GAP43-GCaMP6m, 4.83 ± 0.78; nADR of u-GCaMP6m, 0.76 ± 0.08; $P = 3.09 \times 10^{-5}$; Fig. 1c). The GAP43 motif also targeted GCaMP6s and GCaMP6f to axons with equally

[1]Department of Biochemistry and Molecular Medicine, University of California Davis, Davis, CA, USA. [2]Janelia Research Campus, Howard Hughes Medical Institute, Ashburn, VA, USA. [3]Champalimaud Center for the Unknown, Lisbon, Portugal. [4]Department of Physics, Department of Molecular & Cellular Biology, University of California Berkeley, Berkeley, CA, USA. [5]Westlake Institute for Advanced Study, Hangzhou, China.
*e-mail: leopoldo.petreanu@neuro.fchampalimaud.org; lintian@ucdavis.edu

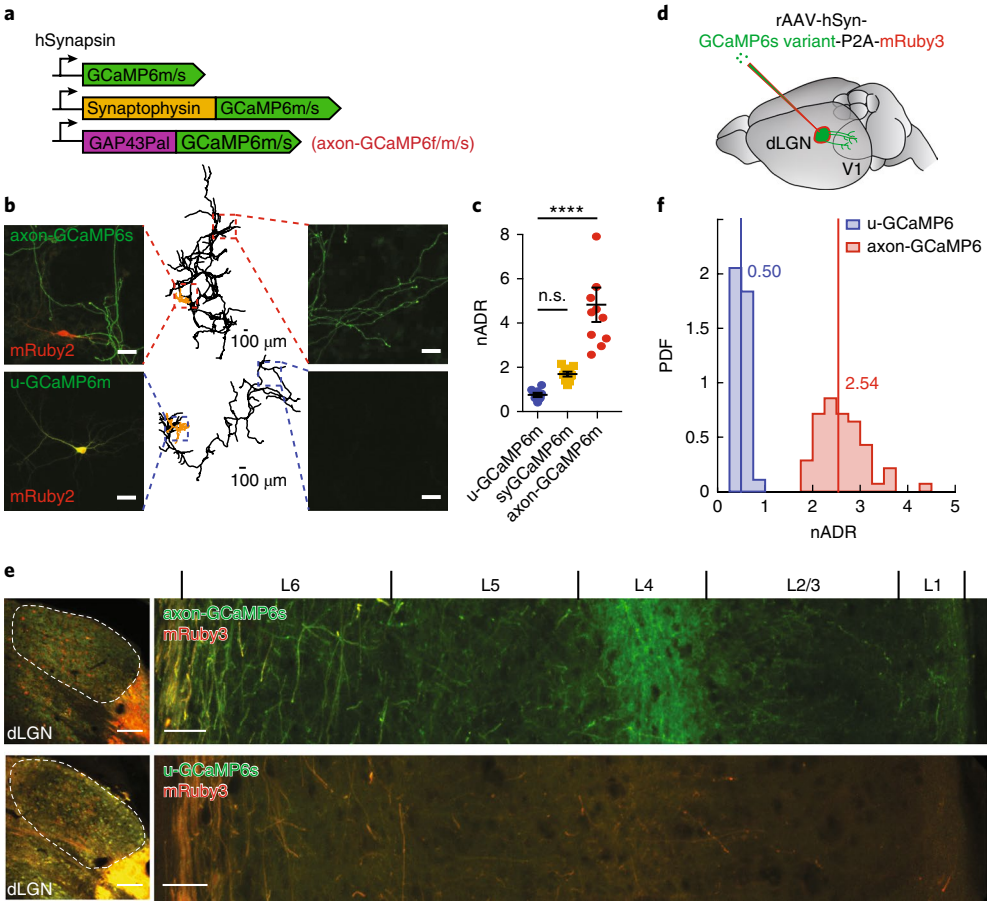

Fig. 1 | Axonal enrichment of GCaMP sensor driven by GAP43 targeting motif in dissociated cells and in vivo. a, Schematic representation of u-GCaMP6 (type m or s), syGCaMP6 (type m or s), and axon-GCaMP6 (type f, m, or s). **b**, Representative images showing enhanced axon localization of axon-GCaMP6m compared to u-GCaMP6m in dissociated neuronal culture. Results were found to be consistent across three different cultures per construct. Scale bars, 20 µm (insets); 100 µm (cell traces). **c**, Normalized nADR (see Methods for description). Average nADRs of axon-GCaMP6m (4.83 ± 0.78) represent an approximate fivefold increase compared to u-GCaMP6m (0.76 ± 0.08) or syGCaMP6m (1.77 ± 0.11; $F_{2,27} = 26.52$, $P = 8.36 \times 10^{-7}$, n.s. = 0.23, $^{****}P = 3.09 \times 10^{-5}$, respectively; one-way ANOVA with Tukey–Kramer multiple-comparisons test; $n = 8$–10 cells from three cultures for each construct). **d**–**f**, Characterization of nADR of thalamocortical axons in V1. (**d**) Schematic representation of viral injection site of AAV encoding bicistronic constructs in mouse dLGN. (**e**) Representative images showing densely labeled L4 axons projected from dLGN labeled with axon-GCaMP6s, whereas cell somata were nearly devoid of labeling. Results were consistent across four animals per construct. Scale bars, 100 µm (cortex); 500 µm (thalamus). (**f**) Probability-density histogram (PDF) of nADR values derived for both constructs with medians indicated by vertical line (axon-GCaMP6s, 2.54 ± 0.28; u-GCaMP6s, 0.50 ± 0.06; $P = 4.37 \times 10^{-16}$; Wilcoxon's rank-sum test; $n = 56$ slices for axon-GCaMP6s and $n = 37$ slices for u-GCaMP6s, from 3 animals per construct). Data are presented as mean ± s.e.m.

increased nADR compared with GCaMP6m (nADR of GAP43-GCaMP6s, 5.65 ± 1.03; nADR of GAP43-GCaMP6f, 4.58 ± 0.44; $P = 8.72 \times 10^{-5}$ and $P = 2.19 \times 10^{-6}$, respectively). In contrast, direct tethering to a presynaptic protein (i.e., Synaptophysin-GCaMP[15] or syGCaMP), as previously reported, only moderately targeted the probe to axons, producing about a twofold increase compared to u-GCaMP6m (nADR: 1.70 ± 0.11, $P = 0.23$). The GAP43-fused GCaMP6m showed rapid enrichment in axons as early as 2 d post-transfection, remained stable across 5 d (Supplementary Fig. 1c), and displayed more consistent labeling across axonal arbors than u-GCaMP6m or syGCaMP6m (Supplementary Fig. 1d,e). We refer to GAP43-fused GCaMP6 as 'axon-GCaMP6' and further characterized it in vivo.

We next sought to determine the targeting efficiency of axon-GCaMP6 in long-range axons in vivo. We engineered bicistronic constructs encoding either axon-GCaMP6s or u-GCaMP6s followed by a P2A peptide-fused untargeted red fluorophore (mRuby3)[26], such that red fluorescence allowed normalization of expression levels (Fig. 1d). We labeled neurons in dorsal lateral geniculate nucleus of the thalamus (dLGN) with recombinant adeno-associated virus (rAAV) encoding axon-GCaMP6s-P2A-mRuby3 or u-GCaMP6s-P2A-mRuby3. We achieved similar patterns and levels of transduction of red fluorescence using both viruses (Supplementary Figs. 2 and 3). Strikingly, in animals injected with axon-GCaMP6s-P2A-mRuby3, we found that somata and dendritic arbors of dLGN neurons were essentially devoid of green fluorescence after 2 weeks of expression, while the axons of this cell population were brightly labeled in primary visual cortex (V1; Fig. 1e). To calculate nADR, we calculated the ratio of green fluorescence from dLGN axons in layer 4 (L4), the primary target of the dLGN axons within V1, to those from somata within dLGN and normalized them to the ratio of red fluorescence. Similarly to what we observed in dissociated neuronal culture, axon-GCaMP6s displayed about a fivefold increase to nADR over u-GCaMP6s (axon-GCaMP6s, 2.54 ± 0.28; u-GCaMP6s, 0.50 ± 0.06; $P = 4.37 \times 10^{-16}$; Fig. 1f). These data suggested that axon-GCaMP6s is actively transported into distal axons.

We then sought to characterize the photostability and diffusibility of axon-GCaMP6m using fluorescence loss in photobleaching

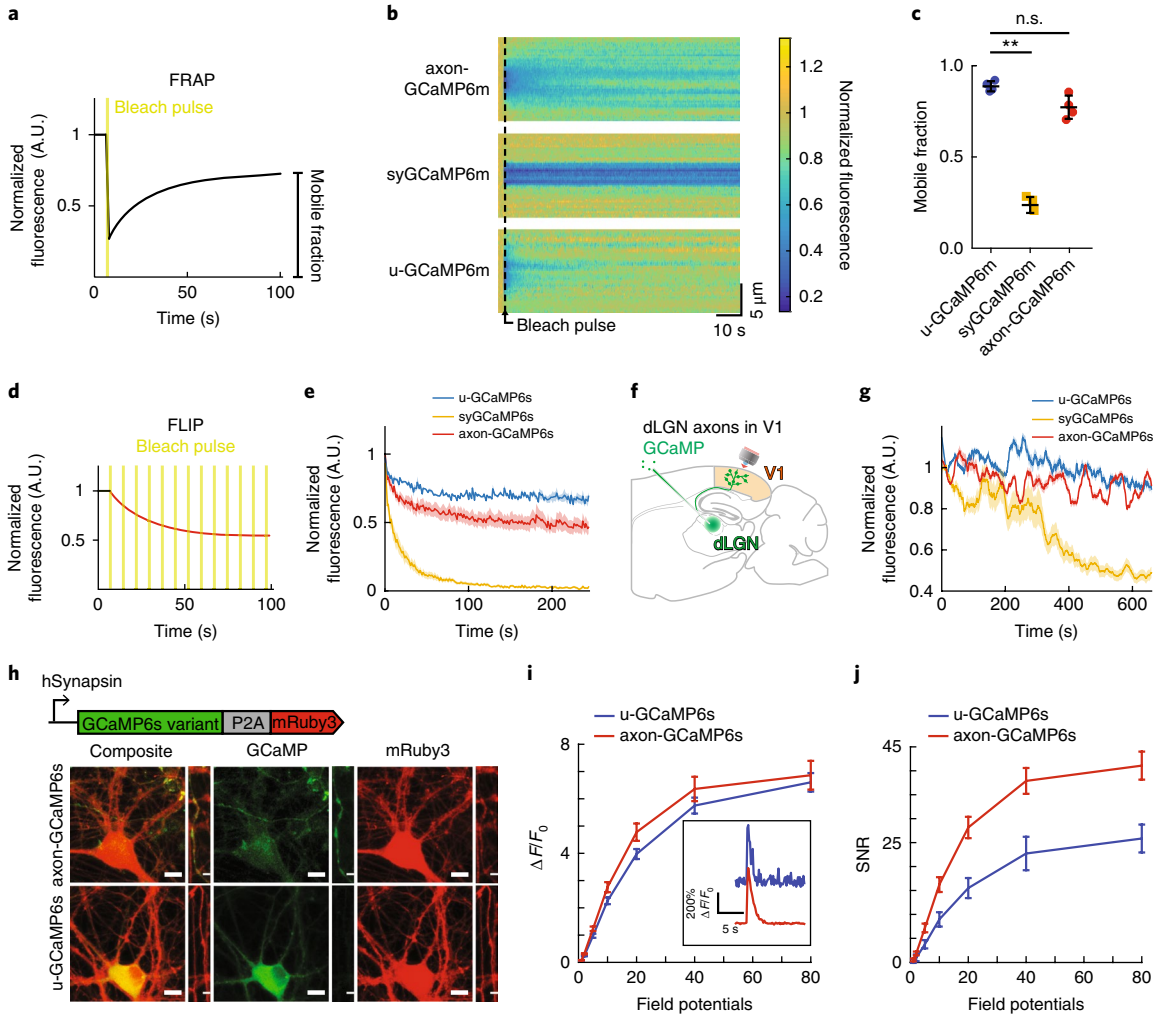

Fig. 2 | Axon-GCaMP maintains photostability and displays enhanced SNR. a–e, Characterization of photostability and diffusibility. Schematic representation of the (**a**) fluorescence recovery after photobleaching (FRAP) and (**d**) fluorescence loss in photobleaching (FLIP) experiments. (**b**) Representative pseudo-linescans from u-GCaMP6m, axon-GCaMP6m, and syGCaMP6m FRAP demonstrated rapid recovery of fluorescence for u-GCaMP6m and axon-GCaMP6m, but not for syGCaMP6m. Experiment was repeated on two independent cultures per construct with similar results. (**c**) Mobile fractions of u-GCaMP6m, syGCaMP6m, and axon-GCaMP6m as assessed by FRAP ($\chi^2_{2,11} = 9.85$, $P = 0.0073$, n.s. = 0.26, $^{**}P = 0.0048$, respectively; Kruskal–Wallis test with Dunn's test for multiple comparisons; $n = 4$ cells from 2 plates per construct). Data plotted as mean ± s.e.m. (**e**) Time course of normalized fluorescence intensity changes during FLIP experiments. Data plotted as mean (solid line) ± s.e.m. (shaded regions); $n = 3$ cells per construct. **f**,**g**, Characterization of photostability in vivo. (**f**) Schematic representation of viral injection in dLGN followed by in vivo imaging axons projecting to V1. (**g**) Time course of fluorescence intensity normalized to the first 50 s of acquisition during imaging of dLGN projection. Data plotted as mean (solid line) ± s.e.m. (shaded regions); $n = 377$, 70, and 236 for u-GCaMP6s, syGCaMP6s, and axon-GCaMP6s, respectively. Individual traces were smoothed by a 100-timepoint boxcar filter to emphasize low-frequency components of data. **h**, Top: schematic representation of bicistronic constructs expressed in dissociated neuronal culture. Bottom: representative images showing increased green fluorescence in axons when labeled with axon-GCaMP6s, whereas u-GCaMP6s primarily labels somatodendritic compartments of neurons. Experimental data was derived from 3 independent cultures per construct with similar results. Scale bars, 10 µm (somatic image), 3 µm (axonal image). **i**,**j**, Average (**i**) $\Delta F/F$ and (**j**) SNR in response to indicated number of field-potential stimuli. Inset: reduced baseline noise in single-trial time-lapse traces of axon-GCaMP6s in response to 20 field potential stimuli. Data plotted as mean peak values ± s.d.; $n = 9$ imaging sessions from 3 transductions per construct.

and fluorescence recovery after photobleaching assays (Fig. 2a,d and Supplementary Fig. 4a–e). Axon-GCaMP6m diffused rapidly between adjacent axonal compartments at a rate similar to that of u-GCaMP6m (mobile fraction of axon-GCaMP6m, 0.77 ± 0.02; mobile fraction for u-GCaMP6m, 0.90 ± 0.03; Fig. 2b,c and Supplementary Fig. 4d,e). High diffusibility led to fast replenishment of bleached molecules, thus greatly reducing effective photobleaching of axon-GCaMP6m (Fig. 2e). In contrast, syGCaMP6m displayed significantly reduced diffusibility, resulting in rapid photobleaching consistent with previous in vivo observations[16] (mobile fraction for syGCaMP6m, 0.28 ± 0.01; Fig. 2c,e and Supplementary Fig. 4c). Additionally, the dipalmitoylation modification of axon-GCaMP6m provided better photostability than some of the other targeting motifs that contained either myristoylation domains (for example, Lck) or multiple binding sites for transport effectors (for example, myosin VI binding domain), which is consistent with previously reported results[27] (Supplementary Fig. 4c).

To confirm that axon-GCaMP is more photostable in vivo, we labeled dLGN with rAAV encoding u-GCaMP6s, syGCaMP6s, or axon-GCaMP6s (Fig. 2f), followed by continuous two-photon

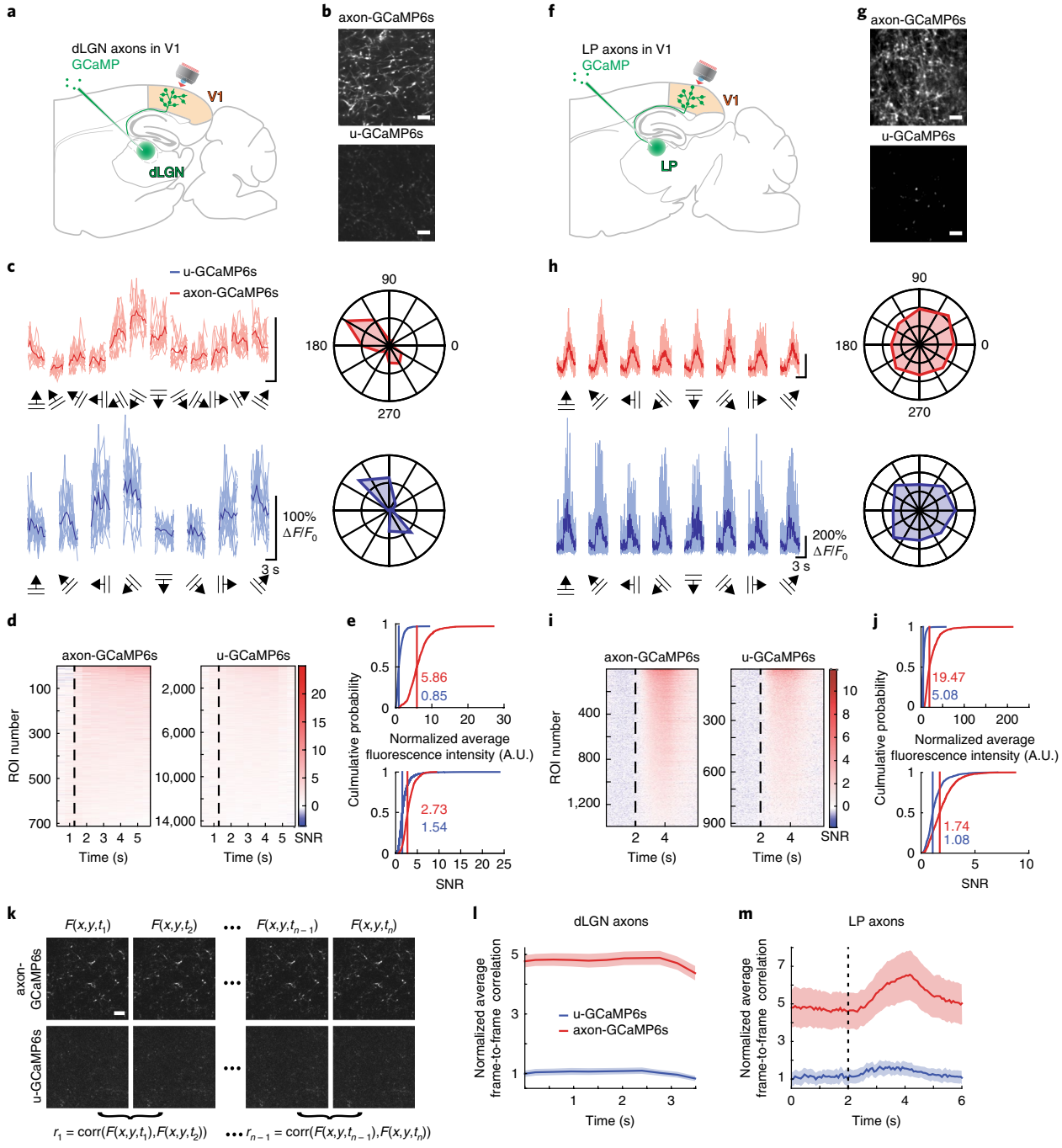

Fig. 3 | Axon-GCaMP6s improves SNR and image-wise correlations in long-distance axons. a,**f**, Schematic representation of viral injection in (**a**) dLGN and (**f**) LP, followed by in vivo imaging in V1 of projected axons. **b**,**g**, Representative images of L1 axons projected from (**b**) dLGN and (**g**) LP, demonstrating enhanced brightness of axon-GCaMP6s expressing axons. Experiments were performed in at least 3 animals per construct injection site pair with similar results. Scale bars,10 µm. **c**,**h**, Left: fluorescence of a representative ROI in response to the indicated grating directions (10 trials per direction) of axon-GCaMP6s and u-GCaMP6s in (**c**) dLGN and (**h**) LP. Data presented with averages in dark colors and individual trials in light colors. Scale bars, 3 s; 100% $\Delta F/F$. Right: polar plots of tuning properties of the selected ROIs. **d**,**i**, Trial-averaged traces of SNR time courses from all responsive ROIs to preferred stimulus direction. Point at which moving stimulus was presented indicated by vertical dotted black line. **e**,**j**, Top: cumulative distribution of normalized fluorescence intensity of axon-GCaMP6s and u-GCaMP6s in (**e**) dLGN and (**j**) LP axons projecting to V1 (dLGN: axon-GCaMP6s, 5.85; u-GCaMP6s, 0.85; LP: axon-GCaMP6s, 19.47; u-GCaMP6s, 5.08; $P = 2.15 \times 10^{-259}$ and $P = 1.24 \times 10^{-319}$, respectively, Kolmogorov–Smirnov test). Bottom: cumulative distribution of SNRs of individual ROIs with median values indicated by vertical lines and color-coded numeric values (dLGN: axon-GCaMP6s, 2.73; u-GCaMP6s, 1.54; LP: axon-GCaMP6s, 1.07; u-GCaMP6s, 0.64; $P = 9.56 \times 10^{-130}$ and $P = 1.13 \times 10^{-95}$, respectively, Kolmogorov–Smirnov test). In **e**, $n = 712$ ROIs from 4 animals for axon-GCaMP6s and $n = 14{,}478$ ROIs for u-GCaMP6s from 19 animals. For **j**, $n = 1{,}393$ ROIs from 3 animals for axon-GCaMP6s and $n = 917$ ROIs from 4 animals for u-GCaMP6s. **k**–**m**, Axon-GCaMP6s improves frame to frame correlations. (**k**) Representative frames from 1 imaging session per construct in L1 dLGN experiments, showing enhancements to image structure for axon-GCaMP6s. Text above and below the images indicates the procedure for calculating the frame-to-frame correlations. Scale bar, 10 µm. (**l**,**m**) Axon-GCaMP6s permits substantially improved frame-to-frame correlations for image registration. Time course of image-wise correlation values for (**l**) dLGN and (**m**) LP boutons. Data plotted as mean (solid line) ± s.e.m. (shaded regions); $n = 6$ imaging sessions from two animals for each construct.

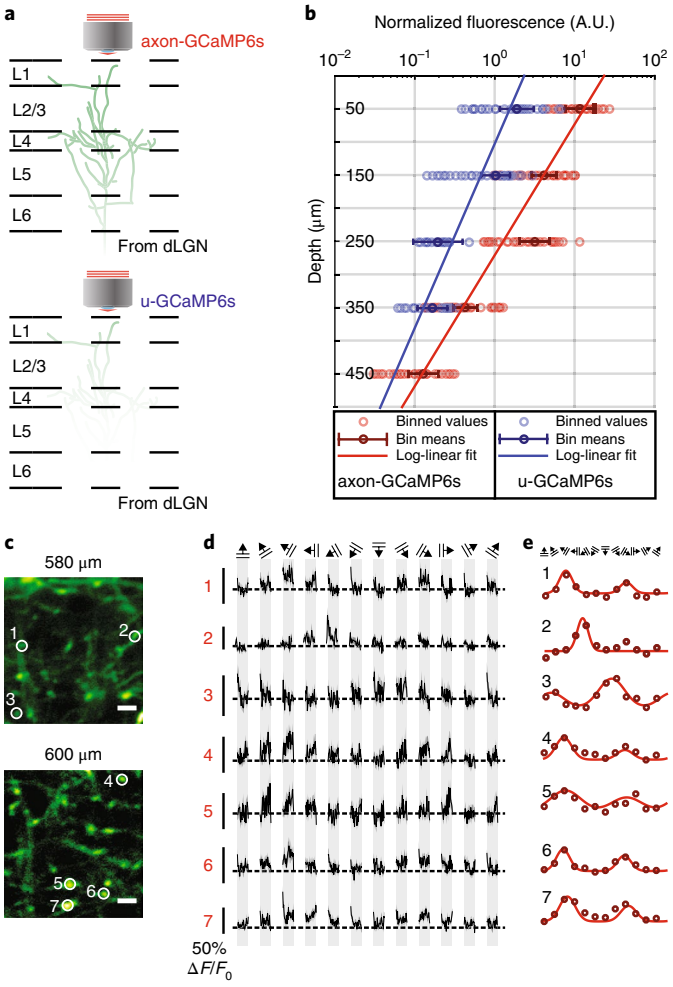

Fig. 4 | Imaging thalamocortical afferents deep in cortical tissue with axon-GCaMP6s. a, Experimental schematic demonstrating that brighter axon-GCaMP6s axons can be imaged at deeper layers within tissue than u-GCaMP6s axons. **b**, Comparison of axon-GCaMP6s and u-GCaMP6s fluorescence normalized to the square of the excitation laser power, as a function of imaging depth. Data plotted as individual ROIs with binned values (light color), binned means ± s.e.m. (dark colors), and log-linear fit across the depth ($F_{1,1,396}$) = 1,242.35, $P < 4.94 \times 10^{-324}$, ANCOVA). For u-GCaMP6s we analyzed 500 ROIs from 2 imaging sessions per depth from each of 4 animals; for axon-GCaMP6s we analyzed 900 ROIs from 2 imaging sessions per depth from 3 animals. **c**, Representative images of dLGN axons projecting to V1 with numbered circles indicating analyzed ROI locations at 580 μm (top) and 600 μm (bottom) below pia. Results were similar across 3 tested animals. Scale bars, 3 μm. **d**,**e**, Response properties of individual ROIs deep in tissue. (**d**) Average $\Delta F/F$ traces aligned to stimulus direction of ROIs indicated in **c**, with baseline indicated by dotted black line. Data plotted as mean (black line) ± s.e.m. (gray shading); $n = 10$ trials per direction. (**e**) Tuning curves for individual ROIs.

excitation through a cranial window in awake, behaving animals. Upon hundreds of seconds of illumination, the fluorescence of dLGN projections in superficial V1 labeled with either u-GCaMP6s or axon-GCaMP6s remained largely unchanged (Fig. 2g and Supplementary Fig. 4f). In contrast, the fluorescence signals of syGCaMP6s-labeled projections decreased by more than 50% during the initial 400 s of illumination (Fig. 2g and Supplementary Fig. 4f).

Finally, we characterized the sensitivity of axon-GCaMP6 in response to field-potential stimuli. We transfected axon-GCaMP6s-P2A-mRuby3 or u-GCaMP6s-P2A-mRuby3 into cultured hippocampal neurons. After 5 d of expression in dissociated neuronal culture, the ratio of green-to-red fluorescence of axons expressing axon-GCaMP6s was about fivefold higher than those labeled with u-GCaMP6s (axon-GCaMP6s, 0.100; u-GCaMP6s, 0.023; Fig. 2h and Supplementary Fig. 5a). In response to a variety of field-potential stimuli (30 Hz), fluorescence changes ($\Delta F/F_0$) of axon-GCaMP6s were similar to those of u-GCaMP6s, with higher basal fluorescence levels (Supplementary Fig. 5b) and lower noise, resulting in ~twofold enhancement in SNR (for details, see Methods) across all stimuli (Fig. 2i,j and Supplementary Fig. 5b). Kinetics (Supplementary Fig. 5c,d), size of detected regions of interest (ROIs, ~0.5–10 μm²)[28] (Supplementary Fig. 5e,f), and fluorescence brightness from the secondary fluorophore, mRuby3 (Supplementary Fig. 5g,h), were similar between axon-GCaMP6s and u-GCaMP6s. We therefore conclude that increased probe enrichment in axons was the primary driver of the observed enhancement to SNR displayed by axon-GCaMP6s.

In vivo imaging of distal afferent calcium signals with axon-GCaMPs. We sought to determine whether improved properties of axon-GCaMP6 could enable in vivo applications that are difficult with u-GCaMP. Thalamocortical projections to sensory cortices, such as those projected from dLGN and lateral posterior nucleus of the thalamus (LP), are dimly labeled by u-GCaMPs[9,11,12]. To determine the effect of axonal enrichment on SNR, we stimulated mice with drifting gratings and imaged the responses of dLGN cells (Fig. 3a–e and Supplementary Fig. 6a–c) and LP cells (Fig. 3f–j and Supplementary Fig. 6d–f) at their axon terminals in layer 1 (L1) of V1.

We successfully recorded calcium signals in thalamocortical axons in superficial layer of V1 in response to drifting grating stimuli[11,12] (Fig. 3c,h). Axons labeled with axon-GCaMP6s displayed a ~sevenfold increase in normalized basal green fluorescence over u-GCaMP6s for dLGN axons (5.86 for axon-GCAMP6s, 0.85 for u-GCaMP6s; $P = 2.15 \times 10^{-259}$). LP axons similarly showed a ~fourfold increase (19.47 for axon-GCaMP6s, 5.08 for u-GCaMP6s; $P = 1.24 \times 10^{-319}$; Fig. 3b,e,g,j and Supplementary Video 1). While u-GCamP6s-expressing axons displayed bright fluorescent varicosities that are likely boutons[6,7,29], axon-GCaMP6s fluorescence was relatively homogenous in both axonal shafts and varicosities (Fig. 3b,g). Because signal amplitude is generally lower in the axonal shaft than in varicose structures (Supplementary Fig. 7; see also ref. [29]), we drew ROIs over varicosities (for details, see Methods) and measured visual responses of thalamocortical axonal populations. SNR (for details, see Methods) of axon-GCaMP6s in response to drifting gratings was significantly improved for dLGN axons (2.73 for axon-GCAMP6s, 1.54 for u-GCaMP6s; $P = 9.56 \times 10^{-130}$) as well as LP axons (1.57 for axon-GCaMP6s, 0.98 for u-GCaMP6s; $P = 1.13 \times 10^{-95}$; Fig. 3d,e,i,j). Consistent with our dissociated neuronal culture data, similar $\Delta F/F_0$ values were observed across both constructs for dLGN axons (0.72 for axon-GCAMP6s, 0.40 for u-GCaMP6s; $P = 5.41 \times 10^{-73}$) and LP axons (0.86 for axon-GCaMP6s, 0.83 for u-GCaMP6s; $P = 0.44$; Supplementary Fig. 6b,c,e,f).

We next compared the sensitivity of axon-GCaMP6s with syGCaMP6s. Because syGCaMP6s bleaches more rapidly than other GCaMP6s designs (Supplementary Figs. 4f and 8a–c), we observed trial-number-dependent rundown of $\Delta F/F$ and SNR values (Supplementary Fig. 8c–e). We then compared the brightness of ROIs only in the first 25 s of imaging. At this early period of the imaging session, brightness of axon-GCaMP6s was less than twofold higher than that of syGCaMP6s (5.57 for axon-GCaMP6s, 3.45 for syGCaMP6s; $P = 3.13 \times 10^{-19}$; Supplementary Fig. 8f,g). When averaged across all trials, syGCaMP6s exhibited comparable $\Delta F/F$ values (0.72 for axon-GCaMP6s, 0.65 for syGCaMP6s; $P = 0.016$) and significantly lower SNRs (2.73 for axon-GCaMP6s, 1.63 for

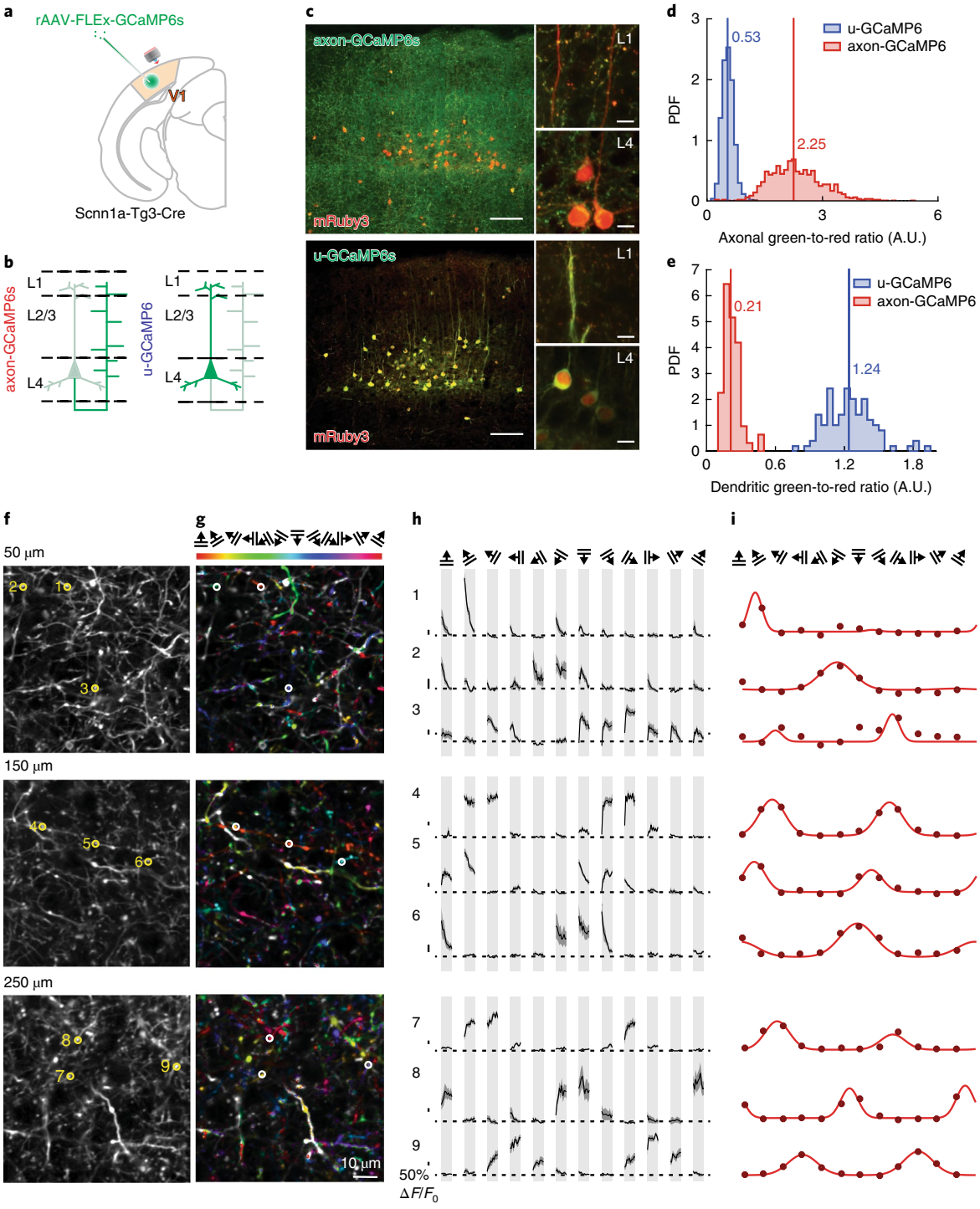

Fig. 5 | Axon-GCaMP6s permits layer-specific recording of axons projected from local neurons, without contamination from somatodendritic signals. a, Schematic representation of labeling L4 neurons with Cre-dependent rAAV encoding axon-GCaMP6s or u-GCaMP6s in Scnn1a-Cre-Tg3 mice. **b**, Expected pattern of transduction: axon-GCaMP6s strongly labeling axons, with weak labeling in the somatodendritic compartment, and the reverse pattern for u-GCaMP6s. **c**, Representative images showing expression patterns of axon-GCaMP6s (top) or u-GCaMP6s (bottom) fused to P2A-mRuby3. Axon-GCaMP6s is enriched in axons, whereas u-GCaMP6s more strongly labels somatodendritic compartments. Inset: representative zoomed-in images in L1 and L4. This result was consistently found in 2 animals per construct. Scale bar, 100 μm (somatic image), 10 μm (inset). **d**,**e**, Probability-density histograms of green-to-red ratio at (**d**) axons or (**e**) dendrites. Distribution medians indicated by vertical lines. Axon-GCaMP6s displayed significantly enhanced green-to-red ratio in axons, but dramatically decreased green-to-red ratio in dendrites, compared to u-GCaMP6s ($P < 4.94 \times 10^{-324}$ and $P = 1.57 \times 10^{-26}$, respectively; Wilcoxon's rank-sum test; $n = 1{,}200$ ROIs from 2 animals for both constructs). **f**–**i**, Axon-GCaMP6s enabled layer-specific tuning properties of axons across cortical layers in V1. Data were derived from 2 imaging sessions per depth in 2 animals. (**f**) Representative images of axons at indicated depth with numbered circles indicating analyzed ROIs. (**g**) Color-coded tuning map demonstrating pixel-wise tuning across analyzed images. (**h**) Average $\Delta F/F$ traces aligned to stimulus direction of individual ROIs, with baseline indicated by dotted black line. Data plotted as mean (black line) ± s.e.m. (gray shading); $n = 10$ trials per direction. (**i**) Tuning curves for individual ROIs.

syGCaMP6s; $P = 1.14 \times 10^{-25}$) than axon-GCaMP6s (Supplementary Fig. 8h–k).

In addition, we examined axonal enrichment and SNR of GCaMP6f when fused to the GAP43 targeting motif. As expected, we observed a ninefold increase in normalized basal green fluorescence (5.99 for axon-GCaMP6f, 0.60 for u-GCaMP6f; $P = 9.87 \times 10^{-98}$) and a 1.5-fold increase in SNR over u-GCaMP6f for dLGN axons (1.27 for axon-GCaMP6f, 0.78 for u-GCaMP6f; $P = 1.20 \times 10^{-9}$, Kolmogorov–Smirnov test; Supplementary Fig. 9).

We did not observe significant differences in population orientation or direction preference between axon-GCaMP6s- and u-GCaMP6s-labeled thalamocortical axons ($F_{1, 275} = 0.001$, $P = 0.97$; Supplementary Fig. 10a–f). Further, the response kinetics was not perturbed beyond what would be expected for higher levels of GCaMP indicator expression[30] (Supplementary Fig. 10g–i). Together, these data suggest that axon-GCaMP6s expression did not alter neuronal physiology. Our data thus show that axon-GCaMP6s enriches in long-range axons, resulting in enhanced SNR in vivo without interfering with circuit properties.

Axon-GCaMP6 can also be efficiently expressed in short, corticocortical projections at early timepoints following viral induction, when u-GCaMP is only minimally expressed (Supplementary Fig. 11a). Two weeks after injection of u-GCaMP6s or axon-GCaMP6s virus into lateromedial (LM) visual cortex, we observed minimal expression of u-GCaMP6s in LM axons in V1, and only 20% of analyzed ROIs were visually responsive. In contrast, axon-GCaMP6s enriched in axons, displaying bright axonal and bouton labeling, with 80% of axons responding to visual stimuli. The SNR was increased threefold (1.09 for axon-GCaMP6s, 0.35 for u-GCaMP6s; $P = 5.62 \times 10^{-12}$), while $\Delta F/F_0$ showed a twofold improvement (0.65 for axon-GCaMP6s, 0.30 for u-GCaMP6s; $P = 1.06 \times 10^{-7}$; Supplementary Fig. 11), suggesting that active transportation of axon-GCaMP6 allows imaging at earlier timepoints in axons.

The enhanced brightness and photostability offered by axon-GCaMP6 permitted robust cross-correlation-based correction of motion artifacts in axonal structures (Fig. 3k–m). Motion artifacts plague imaging experiments in awake, behaving animals, but are usually correctable (at least in part) with brightly labeled cell bodies. Image registration in axons is especially challenging if the axons are only dimly labeled, particularly as axons are tiny and can easily move within the imaging plane. These difficulties are especially pronounced at commonly used acquisition speeds, leading to limited photon budgets and poorly defined structural information for performing motion correction. As such, axonal motion artifacts are frequently uncorrectable. The increased brightness and photostability of axon-GCaMP6s at distal axons (Fig. 3b,e,g,j and Supplementary Fig. 11b,f) greatly increased frame-to-frame correlations relative to u-GCaMP6s (five- to tenfold; correlations normalized to uGCaMP6s: dLGN axons, 4.83; LP axons, 4.76; LM axons, 10.41; Fig. 3k–m and Supplementary Fig. 11e), allowing efficient motion-artifact correction in axonal structures[31].

Axon-GCaMP enables imaging of thalamic boutons in deep cortical layers in vivo. The small size and dim fluorescence of axons and boutons similarly presents difficulties for imaging deep structures, such as in the subgranular layers of cortex. Even with adaptive optics, tuning properties of thalamic axons are difficult to obtain more than 400 µm below the pia using u-GCaMP6s[11]. As a comparison, boutons of axons projecting from dLGN to the supra- and subgranular layers of V1 were imaged with u-GCaMP6s and axon-GCaMP6s in headfixed, awake mice. Average fluorescence intensity was recorded in 100-µm bins down to 500 µm below pia and normalized to the square of the excitation laser power (Fig. 4a,b). Axon-GCaMP6s was brighter (Fig. 4b) while providing better contrast (Supplementary Fig. 12) than u-GCaMP6s at all depths. This enhanced brightness facilitated the first recordings of dLGN L5/6 axons at depths down to 600 µm (Fig. 4c–e). Orientation-specific fluorescence transients ($\Delta F/F_0$) were clearly observable, and from these transients, we calculated orientation tuning curves of these deep cortical axons (Fig. 4c–e). Similarly, axon-GCaMP6f was also brighter at all depths than u-GCaMP6f. Especially at 600 µm, axon-GCaMP6f allowed for effective recordings of orientation-specific tuning, whereas no fluorescence signal sources were observable with u-GCaMP6f (Supplementary Fig. 13). Thus, axon-GCaMP6 allows in vivo interrogation of previously inaccessible axons deep within tissue.

Axon-GCaMP enables layer-specific imaging of local afferents in vivo. Lastly, we used a Cre-dependent axon-GCaMP6 to record orientation and direction tuning of axons projecting from L4 V1 neurons in each recipient cortical layer without contamination of signal from somatodendritic sources (Fig. 5). L4 excitatory neurons were labeled in Scnn1a-Tg3-Cre mice using rAAV encoding FLEx-axon-GCaMP6s-P2A-mRuby3 or FLEx-GCaMP6s-P2A-mRuby3 driven by the human *Synapsin1* promoter (Fig. 5a,b). Three weeks after infection, we observed L4 axons labeled with axon-GCaMP6s ramifying across all cortical layers, whereas u-GCaMP6s primarily labeled the somatodendritic compartments of L4 neurons (Fig. 5c). L4 axons and boutons were easily identifiable from intermingled dendritic structures within different cortical layers (Fig. 5c). The average green-to-red ratio of axon-GCaMP6s in axons was about fivefold higher than that of u-GCaMP6s (axon-GCaMP6s, 2.25; u-GCaMP6s, 0.53; $P < 4.94 \times 10^{-324}$; Fig. 5d). In contrast, the green-to-red ratio of axon-GCaMP6s in dendrites was sixfold lower compared to u-GCaMP6s, indicating specific axonal enrichment of axon-GCaMP6s (axon-GCaMP6s, 0.21; u-GCaMP6s, 1.24; $P = 1.57 \times 10^{-26}$; Fig. 5e).

In agreement with our histological results, no dendritic structures were observed in the in vivo two-photon fields of view (Fig. 5f and Supplementary Fig. 14a). In contrast, animals transduced by u-GCaMP6 showed numerous intermingled dendritic structures (Supplementary Fig. 14b). Using axon-GCaMP6s, we were able to readily detect the response (Fig. 5g–i) and calculate the orientation-tuning properties of individual boutons from L4 neurons throughout their projection fields across cortical depths down to 600 µm (Fig. 5i and Supplementary Fig. 15).

In addition, axon-GCaMP6s permits layer-specific output recording of axons projected from other cortical layers as well. When rAAV-hSynapsin-FLEx-axon-GCaMP6s was introduced to V1 of Rbp4-Cre or Ntsr1-Cre driver mouse lines to restrict expression to L5 or L6, respectively, single-bouton tuning properties were clearly detectable in their recipient layers (Supplementary Fig. 14). Thus, axon-GCaMP6s permits recordings of local afferents down to individual boutons even when dendritic structures of transduced cells are present within the same tissue volume.

Discussion

We have overcome the limitations of genetically encoded calcium indicators to allow robust imaging of afferent calcium transients deep in tissue, with structural specificity and with greater SNR. We achieved this by creating an axon-targeted GECI, axon-GCaMP6, which enriches exclusively in local or distal axons with enhanced brightness and photostability, thus expanding calcium imaging beyond the soma and dendrites. Although presynaptic-targeted GCaMPs, such as syGCaMP6, have been developed, imaging with sensors that localize tightly to presynaptic compartments suffers substantially from photobleaching (Fig. 2g). In contrast, axon-GCaMP6 is diffusible, photostable, and displays enhanced SNR. The enrichment of axon-GCaMP6 in axons offers enhanced frame-to-frame cross-correlation without extensive averaging, which greatly facilitates motion correction of axons in vivo.

Axon-GCaMPs enable new applications of calcium imaging with subcellular resolution noninvasively in deep cortical lay-

ers. Thalamic axons ramify in both supra- and subgranular layers. However, in vivo calcium imaging of thalamic boutons has been limited to superficial layers (<400 µm below pia) with untargeted GCaMP6s or GCaMP6f, even with the aid of adaptive optics. With axon-GCaMP6s and axon-GCaMP6f, the tuning properties of individual thalamocortical boutons in subgranular layers can be readily imaged without the aid of adaptive optics while preserving good SNR, which we expect will open the door for new studies of long-range communication in deeper tissue. As an example application, it is now established that infragranular layers, including L5[32,33] and L6[34], receive direct thalamocortical innervation from primary thalamic nuclei. Previous methods have left the axons that form these connections functionally inaccessible. Deeper imaging made possible by axon-GCaMP6 will alleviate this methodological gap.

Finally, we used axon-GCaMP6 to record orientation tuning and direction tuning of layer-specific axonal inputs projected from local neurons, while excluding signal from their extensively intermingled dendritic structures. Recording from local axonal inputs with layer specificity remained difficult, largely due to contamination from intermingled dendritic structures. Generally, it remains unclear what information is provided by local afferents on a layer-by-layer basis. Axon-GCaMP6 allows direct interrogation of these signals with requisite spatial resolution while avoiding contaminating signal from transduced dendrites.

Long-term, high-level expression of GECIs in the mouse brain can result in prolonged response or nonfunctional indicators and can perturb circuit function. In the case of axon-GCaMP6, the enrichment in axons did not perturb neuronal physiology, as evidenced by kinetics and properties of orientation tuning remaining similar to those of untargeted GCaMP6 after long-term expression (4–6 weeks). Although we did not observe adverse effects in our experiments, physiological impact should be carefully examined in each experimental preparation. Possible interference with synaptic physiology should also be examined.

Axon-GCaMP will be useful in a number of other applications and brain regions, and the targeting tag might be transferable to other payloads. The axonal targeting sequence is only 20 amino acids, allowing easy fusion with both red-shifted[35,36] and Förster resonance energy transfer-based GECIs[37–41] or other genetically encoded sensors of neural activity, such as neurotransmitter sensors[42]. Axonal enrichment may be particularly useful for red indicators, as this approach enhances brightness in small subcellular compartments without extensive optimization of basal fluorescence of the indicator itself. In addition, it may be possible to target actuators[43] to axons to allow axon-specific activation of input signals.

Though axon-GCaMP6 is a superior tool for afferent imaging in the mammalian brain, axon-GCaMP6 is not intended as a replacement for monitoring synaptic calcium using syGCaMP. Indeed, syGCaMP indicators have proven their utility for uncovering the coupling between presynaptic calcium and vesicular release in dissociated neuronal cultures[44,45], flies[46], and larval zebrafish[47]. It has also been used to address systems-level questions in the more optically accessible larval zebrafish[48,49]. However, in mouse brain, we observed a high degree of photobleaching of syGCaMP (Fig. 2g), which precludes imaging for longer than a few minutes. When expressed in dissociated neurons, syGCaMP displayed significantly reduced diffusibility ($P = 0.0048$; Fig. 2c), limiting replenishment of photobleached molecules in boutons. The fast photobleaching in vivo is therefore presumably due to slow replenishment of bleached molecules into the imaged volume during prolonged imaging experiments. As the axon-GCaMP targeting strategy maintains fast diffusibility, it is more photostable than syGCaMP6 both in vitro and in vivo.

In vivo, axon-GCaMP6 reports axonal calcium transients in both axonal shafts and putative boutons more effectively than u-GCaMP6. We also observed that fluorescence responses of axon-GCaMP6 in shafts were smaller than those in putative boutons (Supplementary Fig. 7), consistent with previous observations that calcium signals in axons concentrate in the proximity of boutons (see also refs [29,50]). When combined with post hoc structural analysis, it is possible to delineate calcium signals originating in axon shafts or putative boutons. However, when recording afferent signals from specific axons in vivo, interest is often focused on information encoded by axonal signals. Therefore, differentiating signals at synapses versus axons does not usually add additional information for answering questions at the systems level. Axon-GCaMP6 allows more effective analysis of Ca^{2+} signals within axonal shaft compartments, which exhibit signals that are highly correlated with those found in boutons of the same axon[6,14]. As axonal imaging becomes a rich area of research, requiring calcium indicators that are photostable, bright, and capable of specifically reporting axonal signals, we expect that this specialized GCaMP6 will greatly facilitate recordings from afferent signals of any length with subcellular resolution.

Methods

Methods, including statements of data availability and any associated accession codes and references, are available at https://doi.org/10.1038/s41593-018-0211-4.

Received: 13 December 2017; Accepted: 11 July 2018;
Published online: 20 August 2018

References

1. Lin, M. Z. & Schnitzer, M. J. Genetically encoded indicators of neuronal activity. *Nat. Neurosci.* **19**, 1142–1153 (2016).
2. Nakai, J., Ohkura, M. & Imoto, K. A high signal-to-noise Ca(2+) probe composed of a single green fluorescent protein. *Nat. Biotechnol.* **19**, 137–141 (2001).
3. Tian, L. et al. Imaging neural activity in worms, flies and mice with improved GCaMP calcium indicators. *Nat. Methods* **6**, 875–881 (2009).
4. Akerboom, J. et al. Optimization of a GCaMP calcium indicator for neural activity imaging. *J. Neurosci.* **32**, 13819–13840 (2012).
5. Chen, T.-W. et al. Ultrasensitive fluorescent proteins for imaging neuronal activity. *Nature* **499**, 295–300 (2013).
6. Petreanu, L. et al. Activity in motor-sensory projections reveals distributed coding in somatosensation. *Nature* **489**, 299–303 (2012).
7. Glickfeld, L. L., Andermann, M. L., Bonin, V. & Reid, R. C. Cortico-cortical projections in mouse visual cortex are functionally target specific. *Nat. Neurosci.* **16**, 219–226 (2013).
8. Kaifosh, P., Lovett-Barron, M., Turi, G. F., Reardon, T. R. & Losonczy, A. Septo-hippocampal GABAergic signaling across multiple modalities in awake mice. *Nat. Neurosci.* **16**, 1182–1184 (2013).
9. Gambino, F. et al. Sensory-evoked LTP driven by dendritic plateau potentials in vivo. *Nature* **515**, 116–119 (2014).
10. Rothermel, M. & Wachowiak, M. Functional imaging of cortical feedback projections to the olfactory bulb. *Front. Neural Circuits* **8**, 73 (2014).
11. Sun, W., Tan, Z., Mensh, B. D. & Ji, N. Thalamus provides layer 4 of primary visual cortex with orientation- and direction-tuned inputs. *Nat. Neurosci.* **19**, 308–315 (2016).
12. Roth, M. M. et al. Thalamic nuclei convey diverse contextual information to layer 1 of visual cortex. *Nat. Neurosci.* **19**, 299–307 (2016).
13. Kwon, S. E., Yang, H., Minamisawa, G. & O'Connor, D. H. Sensory and decision-related activity propagate in a cortical feedback loop during touch perception. *Nat. Neurosci.* **19**, 1243–1249 (2016).
14. Marques, T., Nguyen, J., Fioreze, G. & Petreanu, L. The functional organization of cortical feedback inputs to primary visual cortex. *Nat. Neurosci.* **21**, 757–764 (2018).
15. Dreosti, E., Odermatt, B., Dorostkar, M. M. & Lagnado, L. A genetically encoded reporter of synaptic activity in vivo. *Nat. Methods* **6**, 883–889 (2009).
16. Walker, A. S., Burrone, J. & Meyer, M. P. Functional imaging in the zebrafish retinotectal system using RGECO. *Front. Neural Circuits* **7**, 34 (2013).
17. El-Husseini, Ael-D., Craven, S. E., Brock, S. C. & Bredt, D. S. Polarized targeting of peripheral membrane proteins in neurons. *J. Biol. Chem.* **276**, 44984–44992 (2001).
18. Padmanabhan, S., Kareva, T., Kholodilov, N. & Burke, R. E. Quantitative morphological comparison of axon-targeting strategies for gene therapies directed to the nigro-striatal projection. *Gene Ther.* **21**, 115–122 (2014).

19. Kline, C. F., Scott, J., Curran, J., Hund, T. J. & Mohler, P. J. Ankyrin-B regulates Cav2.1 and Cav2.2 channel expression and targeting. *J. Biol. Chem.* **289**, 5285–5295 (2014).
20. Aronov, S., Aranda, G., Behar, L. & Ginzburg, I. Axonal tau mRNA localization coincides with tau protein in living neuronal cells and depends on axonal targeting signal. *J. Neurosci.* **21**, 6577–6587 (2001).
21. Zlatkine, P., Mehul, B. & Magee, A. I. Retargeting of cytosolic proteins to the plasma membrane by the Lck protein tyrosine kinase dual acylation motif. *J. Cell Sci.* **110**, 673–679 (1997).
22. Shigetomi, E., Kracun, S., Sofroniew, M. V. & Khakh, B. S. A genetically targeted optical sensor to monitor calcium signals in astrocyte processes. *Nat. Neurosci.* **13**, 759–766 (2010).
23. Lewis, T. L. Jr., Mao, T. & Arnold, D. B. A role for myosin VI in the localization of axonal proteins. *PLoS Biol.* **9**, e1001021 (2011).
24. Kutzleb, C. et al. Paralemmin, a prenyl-palmitoyl-anchored phosphoprotein abundant in neurons and implicated in plasma membrane dynamics and cell process formation. *J. Cell Biol.* **143**, 795–813 (1998).
25. Lewis, T. L. Jr, Mao, T., Svoboda, K. & Arnold, D. B. Myosin-dependent targeting of transmembrane proteins to neuronal dendrites. *Nat. Neurosci.* **12**, 568–576 (2009).
26. Bajar, B. T. et al. Improving brightness and photostability of green and red fluorescent proteins for live cell imaging and FRET reporting. *Sci. Rep.* **6**, 20889 (2016).
27. Hammond, G. R. V., Sim, Y., Lagnado, L. & Irvine, R. F. Reversible binding and rapid diffusion of proteins in complex with inositol lipids serves to coordinate free movement with spatial information. *J. Cell Biol.* **184**, 297–308 (2009).
28. de Chaumont, F. et al. Icy: an open bioimage informatics platform for extended reproducible research. *Nat. Methods* **9**, 690–696 (2012).
29. Koester, H. J. & Sakmann, B. Calcium dynamics associated with action potentials in single nerve terminals of pyramidal cells in layer 2/3 of the young rat neocortex. *J. Physiol. (Lond.)* **529**, 625–646 (2000).
30. Hires, S. A., Tian, L. & Looger, L. L. Reporting neural activity with genetically encoded calcium indicators. *Brain Cell Biol.* **36**, 69–86 (2008).
31. Guizar-Sicairos, M., Thurman, S. T. & Fienup, J. R. Efficient subpixel image registration algorithms. *Opt. Lett.* **33**, 156–158 (2008).
32. Constantinople, C. M. & Bruno, R. M. Deep cortical layers are activated directly by thalamus. *Science* **340**, 1591–1594 (2013).
33. Petreanu, L., Mao, T., Sternson, S. M. & Svoboda, K. The subcellular organization of neocortical excitatory connections. *Nature* **457**, 1142–1145 (2009).
34. Beierlein, M. & Connors, B. W. Short-term dynamics of thalamocortical and intracortical synapses onto layer 6 neurons in neocortex. *J. Neurophysiol.* **88**, 1924–1932 (2002).
35. Zhao, Y. et al. An expanded palette of genetically encoded Ca^{2+} indicators. *Science* **333**, 1888–1891 (2011).
36. Dana, H. et al. Sensitive red protein calcium indicators for imaging neural activity. *eLife* **5**, e12727 (2016).
37. Nagai, T., Yamada, S., Tominaga, T., Ichikawa, M. & Miyawaki, A. Expanded dynamic range of fluorescent indicators for Ca(2+) by circularly permuted yellow fluorescent proteins. *Proc. Natl Acad. Sci. USA* **101**, 10554–10559 (2004).
38. Palmer, A. E. et al. Ca^{2+} indicators based on computationally redesigned calmodulin-peptide pairs. *Chem. Biol.* **13**, 521–530 (2006).
39. Horikawa, K. et al. Spontaneous network activity visualized by ultrasensitive Ca(2+) indicators, yellow Cameleon-Nano. *Nat. Methods* **7**, 729–732 (2010).
40. Mank, M. et al. A genetically encoded calcium indicator for chronic in vivo two-photon imaging. *Nat. Methods* **5**, 805–811 (2008).
41. Thestrup, T. et al. Optimized ratiometric calcium sensors for functional in vivo imaging of neurons and T lymphocytes. *Nat. Methods* **11**, 175–182 (2014).
42. Marvin, J. S. et al. An optimized fluorescent probe for visualizing glutamate neurotransmission. *Nat. Methods* **10**, 162–170 (2013).
43. Zhang, F., Wang, L. P., Boyden, E. S. & Deisseroth, K. Channelrhodopsin-2 and optical control of excitable cells. *Nat. Methods* **3**, 785–792 (2006).
44. Li, H. et al. Concurrent imaging of synaptic vesicle recycling and calcium dynamics. *Front. Mol. Neurosci.* **4**, 34 (2011).
45. Jackson, R. E. & Burrone, J. Visualizing presynaptic calcium dynamics and vesicle fusion with a single genetically encoded reporter at individual synapses. *Front. Synaptic Neurosci.* **8**, 21 (2016).
46. Pech, U., Revelo, N. H., Seitz, K. J., Rizzoli, S. O. & Fiala, A. Optical dissection of experience-dependent pre- and postsynaptic plasticity in the Drosophila brain. *Cell Rep.* **10**, 2083–2095 (2018).
47. Baden, T. et al. A synaptic mechanism for temporal filtering of visual signals. *PLoS Biol.* **12**, e1001972 (2014).
48. Dreosti, E., Esposti, F., Baden, T. & Lagnado, L. In vivo evidence that retinal bipolar cells generate spikes modulated by light. *Nat. Neurosci.* **14**, 951–952 (2011).
49. Johnston, J., Ding, H., Seibel, S. H., Esposti, F. & Lagnado, L. Rapid mapping of visual receptive fields by filtered back projection: application to multi-neuronal electrophysiology and imaging. *J. Physiol. (Lond.)* **592**, 4839–4854 (2014).
50. Cox, C. L., Denk, W., Tank, D. W. & Svoboda, K. Action potentials reliably invade axonal arbors of rat neocortical neurons. *Proc. Natl Acad. Sci. USA* **97**, 9724–9728 (2000).

Acknowledgements

We thank H. Chen at the vector core of vision center at UCD for virus production and L. Looger and B. Mensh for insightful comments on the manuscript. This work was supported by funding to L.T. (DP2MH107056, U01NS090604, and U01NS099714 from the National Institutes of Health and Rita Allen Foundation), to L.P. (Marie Curie PCIG12-GA-2012-334353, the European Union's Seventh Framework Program FP7/2007-2013 under grant agreement No. 600925, and the Champalimaud Foundation), to N.J. (Howard Hughes Medical Institute and grants U01 NS103573 and U01 NS103489 from the National Institutes of Health), and a Human Frontiers Research Grant to L.T. and L.P. (RGY0085/2013).

Author contributions

L.P. and L.T. initiated the project. G.J.B. and L.T. designed the projects; developed axon-targeted GCaMP6; performed characterization of ADR, photostability, and SNR in vitro in dissociated neuronal culture; and performed histological characterization of ADR and expression in vivo. Y.L. G.M., and N.J. performed in vivo characterization of dLGN axons in V1, deep-brain imaging, and layer-specific cortical axonal recording in V1. M.F. and L.P. performed in vivo characterization of L1 axons in V1 projecting from LP and area LM and examined frame-to-frame correlations. G.J.B. analyzed data from in vivo imaging with help from Y.L., M.F., and G.M. E.K.U. performed viral injections. X.X. performed pilot experiments for sensor characterization. G.J.B. and L.T. wrote the manuscript with critical input from all authors.

Competing interests

The authors declare no competing interests.

Additional information

Supplementary information is available for this paper at https://doi.org/10.1038/s41593-018-0211-4.

Reprints and permissions information is available at www.nature.com/reprints.

Correspondence and requests for materials should be addressed to L.P. and L.T.

Publisher's note: Springer Nature remains neutral with regard to jurisdictional claims in published maps and institutional affiliations.

Methods

Protein engineering. All constructs were designed using a combination of overlap extension cloning and gBlock gene fragments (Integrated DNA Technologies). All constructs were flanked by BamHI with a downstream Kozak sequence and start codons, as well as HindIII for final subcloning onto pAAV-hSynapsin1 vectors. Alternatively, constructs were flanked by SacI and AflII sites for subcloning into custom pAAV-hSynapsin1-FLEx vectors.

Concurrent two-color fluorophore expression was achieved by the use of either two plasmids with mRuby2 as the red reference fluorophore or a bicistronic approach in which the GCaMP construct was separated by a P2A sequence[51] from a downstream mRuby3. The two-plasmid approach was used for all in vitro characterization, while the bicistronic approach was used for in vivo characterization. Functional assays were performed with no reference fluorophore.

Dissociated hippocampal neuronal culture. For ADR and diffusion analyses, primary hippocampal neuronal cultures were prepared as described previously[3]. Briefly, P0 or E18 pups were decapitated, and the brains were dissected into ice-cold neural dissection solution (NDS, 10 mM HEPES (Sigma) in Hank's Balanced Salt Solution (HBSS, Thermo Fisher Scientific), pH 7.4). Hippocampi were removed, enzymatically digested with papain (~60 units), washed with prewarmed plating medium (PM, Minimal Essential Medium (Thermo Fisher Scientific) supplemented by 10% FBS (Thermo Fisher Scientific) and 100 U/mL penicillin–streptomycin (Thermo-Fisher Scientific)) and then mechanically digested by trituration. Cells were plated on 35 mm MatTek glass bottom dishes (MatTek) coated with Matrigel matrix (BD Biosciences) or a mixture of poly-L-ornithine (Sigma-Aldrich) and laminin (Sigma-Aldrich), and kept at 37 °C, 5% CO_2 in PM for ~24 h and then in Neurobasal medium (Thermo Fisher Scientific) supplemented by 10% B27 (Thermo Fisher Scientific) for the experiment duration, with half medium exchanges every 4 d. On the fifth day in vitro (DIV), cells used for ADR and FRAP/FLIP experiments were transfected by Effectene (Qiagen), following the manufacturer's recommendations with the following modification: for 100 µL transfection complex, we included only 5 µL Effectene reagent. Such cells were subsequently used for imaging experiments between 2 and 5 d post-transfection. Cells used for SNR analysis were transduced on DIV5 by rAAV-hSynapsin-GCaMP6s-P2A-mRuby3-WPRE-SV40 or rAAV-hSyanspin-axon-GCaMP6s-P2A-mRuby3-WPRE-SV40 to drive near-complete transduction of all cultured neurons. All cultures were imaged on a laser scanning confocal microscope (Zeiss 710) equipped with 405-, 488-, 514-, 561-, and 633-nm laser lines. Band limits for detection of GCaMP fluorescence were set between 493 and 541 nm while collection of mRuby fluorescence was beyond 590 nm. Prior to imaging, cultures were washed and incubated in HBSS containing 2 mM $MgCl_2$ and $CaCl_2$ to minimize background due to fluorescent culture medium components. For experiments requiring field stimulation, an RC-37FS perfusion insert (Warner Instruments) was fitted into the MatTek. During such experiments, spontaneous network activity was suppressed by inclusion of 20 µM of 6-cyano-7-nitroquinoxaline-2,3-dione (CNQX) and 40 µM of D-(-)-2-amino-5-phosphopentanoic acid (D-APV) to the imaging medium. All data collected for quantitative comparisons were collected with identical imaging parameters, except that the laser power was adjusted to just below saturation for the brightest feature of the imaged cell or fields.

Quantification of axon-to-dendrite ratio. Calculation of the normalized ratio was performed following the method of Lewis et al.[25]. Specifically, a non-normalized ratio of fluorescence between the axon and somatodendritic compartments was calculated as

$$uADR = \frac{F_{TestFP,\ Axon}}{F_{TestFP,\ Somatodendritic}}$$

where F_{TestFP} refers to the background-subtracted average fluorescence of GCaMP within the indicated structure. This measure was then normalized to similar values for mRuby2 as

$$nADR = \frac{uADR}{\left(\frac{F_{RefFP,\ Axon}}{F_{RefFP,\ Somatodendritic}}\right)}$$

where F_{refFP} refers to the background-subtracted average fluorescence of mRuby2 within the indicated structure. Normalizing to the distribution of red fluorescence thus controls for differences in diffusivity across different cells.

Fluorescence loss in photobleaching and fluorescence recovery after photobleaching. For FLIP experiments, axonal segments greater than 100 µm from the soma were targeted for imaging. After a baseline of ten images, images were acquired alternating with application of bleaching pulses over a 10-µm circle centered in the imaged frame. The same 488-nm line from a 25-mW argon laser was used as the bleaching excitation with a pixel dwell time of 1.58 µs. Loss of fluorescence was then tracked within a background-subtracted ROI covering the axon within the bleached circle. For these experiments, all fields of view included an axon that was not directly attached to the bleached segment. Fluorescence within this control axon segment was monitored to ensure that imaging did not cause greater than a 5% decrease in baseline fluorescence. Imaging sessions in which the control process fluorescence dropped by greater than this threshold were discarded.

FRAP was also performed to extract diffusion coefficients of axonal GCaMP variants[52]. Imaging and bleaching parameters were identical to those used in the FLIP experiments, except that a single bleaching pulse was applied. To drive sufficient bleaching, experiments were conducted in imaging medium supplemented by 5 µM of the calcium ionophore ionomycin, effectively increasing the extinction coefficient of the GCaMP[5]. Normalized postbleach profiles, $f_{Postbleach}(x)$, were determined by dividing the fluorescence profile directly following the bleaching epoch by that preceding the bleach event. Diffusion occurring between consecutive imaging acquisitions was then corrected for by fitting the effective bleach radius, r_e, and bleach depth, K, of the normalized bleach profile to the equation

$$\widehat{f}_{Postbleach}(x) = 1 - K\ e^{-x^2/r_e^2}$$

FRAP curves were then determined by fitting the recovery time course, $F(t)$, to the equation

$$\widehat{F}(t) = (1-a)(F_0 - F_\infty)\ e^{-t/\tau_{slow}} + a(F_0 - F_\infty)\ e^{-t/\tau_{fast}} + F_\infty$$

where a, F_0, F_∞, τ_{slow} and τ_{fast} are free parameters corresponding to the double exponential fraction, the initial postbleach fluorescence, the steady-state fluorescence recovery level, and the slow and fast exponential recovery rates, respectively. The time to half recovery, $t_{1/2}$, was then determined as the timepoint where $\widehat{F}(t_{1/2}) = \frac{F_\infty - F_0}{2}$. Finally, the diffusion coefficient, D, was recovered using the nominal user selected bleach radius, r_n, with the expression

$$D = \frac{r_e^2 + r_n^2}{8\tau_{1/2}}$$

Characterization of performance in dissociated neuronal culture. To quantify performance of GCaMP-labeled cell culture, we performed electrical field-stimulation experiments in dissociated hippocampal culture. In cultures densely transduced by virus, confocal imaging was performed on intermingled fields of axons within fields of view more than 100 µm from the nearest visible dendritic segment. Axons imaged for this study were first masked using the mRuby3 fluorescence signal. These masks were segmented using an ICY plugin to split ROI[28] into ROIs with normal distribution and mean size around that of typical ROIs used in in vivo imaging experiments (0.8–10 µm^2). Time-lapse calcium imaging stacks were acquired from these axons based on the GCaMP fluorescence signal. After a 5-s baseline, 1, 2, 5, 10, 20, 40, or 80 field potentials were applied as 1-V, 1-ms square-wave pulses at 30 Hz under the control of Ephus software[53]. mRuby3-based ROIs were then analyzed with the average of the baseline period, F_0, used to calculate the fluorescent transients $\Delta F/F_0$, as $\Delta F/F_0 = (F - F_0)/F_0$. SNR was then calculated as the maximum $\Delta F/F_0$ divided by the s.d. of the baseline period.

Animal procedures. All animal procedures were conducted according to the Portuguese Direcção Geral de Veterinária and the United States National Institutes of Health guidelines for animal research and were approved by the Institutional Animal Care and Use Committee at the University of California, Davis, the Howard Hughes Medical Institute, or the Champalimaud Center for the Unknown. Wild-type mice were used for in vivo functional imaging of visual thalamic axons as well as for LM corticocortical projections (older than P60, C57BL/6J). Scnn1a-Tg3-Cre mice (Jax no. 009613), Rbp4-Cre mice (MMRRC no. 031125-UCD), and Ntsr1-Cre mice (MMRRC no. 030648-UCD) of both sexes (older than P60) were used for in vivo functional imaging of cortical afferents from L4, L5, and L6 neurons, respectively. Sample sizes (numbers of mice, cells and/or boutons) for each experiment are stated in main text.

Viral injections. Injection procedures were essentially identical to those described in refs [6,11] with a few exceptions. Briefly, virus injection was performed using a glass pipette beveled at 45° with a 15- to 20-µm opening and backfilled with mineral oil. A fitted plunger controlled by a hydraulic manipulator (Narashige, MO10; or World Precision Instruments, UMP3) was inserted into the pipette and used to load and inject the viral solution.

For confirmation of enhanced axonal expression of axon-GCaMP6s in living mice, ~20–40 nL of rAAV2/1-hSynapsin1-GCaMP6s-P2A-mRuby3-WPRE-SV40 (~2×10^{13} viral genome (vg) per mL) or rAAV2/1-hSynapsin1-axon-GCaMP6sP2A-mRuby3-WPRE-SV40 (~3.2×10^{13} vg per mL) were slowly injected into dLGN (2.1 mm posterior to bregma; 2.3 mm lateral from midline; 2.5 mm below pia). For axon-specific labeling of local cortical connections in V1, ~20–40 nL of rAAV2/1-hSynapsin1-axon-GCaMP6s-WPRE-SV40 (~1.2×10^{13} vg per mL) were injected to cortical L4 (Scnn1a-Tg3-Cre mice: three injection sites in left

hemisphere centered at 3.4 mm posterior to bregma; 2.7 mm lateral from midline; 0.3 mm below pia; injection sites are ~250 µm apart). Additionally, we produced these viruses under a 2/5 serotype to test differences in transduction efficiency. We did not find apparent differences across serotypes (data not shown).

For calcium imaging of thalamocortical and LM corticocortical projections, ~20–80 nL of rAAV2/1-hSynapsin1-GCaMP6s-WPRE-SV40 (~$2–4\times10^{13}$ infectious units per mL) or rAAV2/1-hSynapsin1-axon-GCaMP6s-WPRE-SV40 solution (~4×10^{13} infectious units per mL) were slowly injected into dLGN, LP (1.9 mm posterior to bregma; 1.4 mm lateral from midline; 2.7 mm below bregma), or LM (coordinates determined by intrinsic optical imaging[54,55]). For imaging of cortical neurons and local axon projections ~20–40 nL of rAAV1-hSynapsin1-FLEx-GCaMP6s-WPRE-SV40 (~2.4×10^{13} infectious units per mL) or rAAV1-hSynapsin1-FLEx-axon-GCaMP6s-WPRE-SV40 (~3.1×10^{12} per mL) were injected per injection site into V1 for cortical L4 (Scnn1a-Tg3-Cre mice), cortical L5 (Rbp4-Cre mice), or cortical L6 (Ntsr1-Cre mice) for somatic or local cortical axon imaging, respectively, at three injection sites in left hemisphere centered at 3.4 mm posterior to bregma; 2.7 mm lateral from midline; 0.4 mm below pia; injection sites were ~250 µm apart. All calcium imaging data of u-GCaMP6$^+$ dLGN axons was first reported by Sun and co-workers[11].

Head plate/cranial window implantation. Craniotomy and head plate implantation were carried out at the same time as virus injection for calcium imaging experiments. A 2.5- to 4-mm diameter craniotomy was made over the left V1 (center: 3.4 mm posterior to bregma; 2.7 mm lateral from midline) of the anaesthetized mice with dura left intact. For experiments using adaptive optical correction of aberration, 2 µL of red fluorescent bead solution (2-µm diameter; 1:500 in saline; Life Technologies, F-8826) was deposited on the dura surface. A glass window made of either a single coverslip (Fisher Scientific no. 1.5) or two coverslips bonded with ultraviolet-cured optical adhesives (Norland Optical Adhesives 61) was embedded in the craniotomy and sealed in place with cyanoacrylate. A titanium headpost was attached to the skull with cyanoacrylate glue and dental acrylic.

Visual stimulation. Visual stimuli were presented on a screen 13–17 cm distant at an angle of ~40° relative to the long axis of the animal on the contralateral side of imaged V1. The stimuli were composed of square gratings with 100% contrast, 0.04–0.07 cycles per degree, drifting at 26° s^{-1}, yielding a temporal frequency of ~2 Hz. For all projections, this stimulus was presented at 8 or 12 different orientations in a pseudorandom sequence. For dLGN recordings, stimuli were 12 s each, of which the stimulus was static for the first and last 3 s and drifted during the middle 6 s. For LP and LM recordings, baseline recordings were acquired for 2 s, during which a gray screen of mean intensity was presented, followed by a drifting grating for 2 s, and finally ending with 2-s presentation of the gray screen. A total of ten trials were presented for each stimulus orientation in the dLGN and LP recordings, and 20 trials were per orientation were presented for LM recordings.

Two-photon imaging. Imaging was performed with two-photon fluorescence microscopes 2–4 weeks after virus injection, when most neurons in dLGN, LP, and cortex exhibited nuclear-excluded expression[5] of GCaMP6s. Recording from LM axons were done 14–16 d after viral injection. For dLGN recordings, mice were headfixed, awake, and restrained. LP and LM recordings were taken in animals lightly anesthetized with 1% isoflurane and an intramuscular injection of chlorprothixene at 1 mg/kg during the imaging period. When imaging awake animals, mice were habituated to experimental handling by being headfixed onto the sample stage with its body restrained under a half-cylindrical cover 1 week after surgery. This procedure was repeated 3–4 times for each animal, and each time for 15–60 min. Each experimental session lasted between 45 min and 3 h. Multiple sections were imaged within the same mouse. GCaMP6 was excited at 900–940 nm with a Ti:sapphire laser (Ultra II, Coherent) or an optical parametric oscillator (InSight DeepSee, Spectra-physics) that was focused by either a Nikon 16×, 0.8 NA or an Olympus 25×, 1.05 NA objective. Emitted fluorescence photons were detected by a photomultiplier tube (H7422PA-40, Hamamatsu).

Axonal images from the brain surface down to up to 600 µm below pia were acquired using custom LabView software or ScanImage5[53]. Images of thalamocortical and corticocortical axons in L1 were taken from 0–80 µm below the pia. For comparison of depth characteristics of u-GCaMP6s and axon-GCaMP6s, imaging fields were binned at 100-µm intervals down to a depth of 450 µm. All imaging areas were confirmed to be in V1 by stereotactic coordinates (3.4 ± 0.6 mm posterior to bregma and 2.7 ± 0.6 mm lateral from midline) or intrinsic signal imaging. Typical images for dLGN and V1 axons had 256×256 pixels, at 0.3 µm per pixel and ~2- to 3-Hz frame rate. Typical images of LP and LM axons were acquired at 512×512 pixels, at 0.3–0.35 µm per pixel with a ~15-Hz frame rate.

Fixed tissue preparation. Following viral injection at timepoints specified within the main text, mice were deeply anaesthetized with isoflurane and transcardially perfused with PBS and then 4% paraformaldehyde (wt./vol.). Brains were removed and postfixed overnight in paraformaldehyde. Coronal brain slices were cut to 30- to 60-µm thickness using a vibratome (V1200S, Leica) or cryostat (CM1860, Leica). Fluorescence images of these sectioned brains were acquired on a laser scanning confocal microscope (Zeiss LSM 710) equipped with 405-, 488-, 514-, 561-, and 633-nm excitation laser lines. Images were collected using the following Plan-Apochromat objectives: 10×, 0.45 NA (optical section step of 2 µm); 20×, 0.8 NA (optical section step of 1.0 µm); 40×, 1.3 NA oil immersion (optical section step of 0.5 µm); and 63×, 1.4 NA oil immersion (optical section step of 0.5 µm). For all calculations of ADR, images were first acquired in the somatic field with laser power set at a level just below saturation of all features in each channel. These same settings were applied during image acquisition in the axonal fields. nADR was then calculated as described in the section "Quantification of dendrite to axon ratio," with somata from an entire slice used as the somatic component and L4 axonal projections used as the axonal component.

In vivo image analysis. Lateral motion artifact in two-photon imaging stacks was corrected using a cross-correlation-based registration algorithm[31], where cross-correlation was used to determine translational shifts in images. In each image stack, the mean projection was used as the registration reference. Several rounds of registration and re-averaging of the stack were performed to decrease $\sum_k (\Delta x_k^2+\Delta y_k^2)$, where Δx_k and Δy_k represent the horizontal and vertical shifts of the kth image, respectively. This process was repeated once for LP and LM data and for up to seven iterations for the dLGN[11] data.

ROI selection. In average or s.d. images of registered image stacks, labeled axons appeared as bright spots in u-GCaMP6 and as filled axonal shafts and varicosities in axon-GCaMP6. For analysis of both u-GCaMP6 and axon-GCaMP6 experiments, circular ROIs (0.8–4 μm^2) were manually drawn over varicosities that likely correspond to presynaptic boutons[11,29].

Characterizing $\Delta F/F$ and SNR in vivo. For stacks derived from LP and LM axons, F_0 was calculated as the average of the baseline fluorescence for each stimulus presentation. For dLGN axons, the mode of the fluorescence intensity histogram from each ROI was used as F_0. Fluorescence transients were then calculated as $\Delta F/F_0=(F-F_0)/F_0$. Averaged $\Delta F/F_0$ traces were then derived from the mean across ten trials of the same orientation. Resultant traces were then averaged over the period of stimulus presentation to derive a $\Delta F/F_0$ value for each ROI. The s.d. of the $\Delta F/F_0$ signal during the period before presenting the moving visual stimulus was calculated across trials, and the resultant values were averaged together. SNR was calculated by dividing the $\Delta F/F_0$ value by the s.d.

To characterize the tuning properties of axonal boutons, we followed the previously described procedure[11]. Briefly, the response R of each ROI to a visual stimulus was defined as the average $\Delta F/F_0$ across the window of drifting gratings. For ROIs with significantly different responses across the drifting directions (one-way ANOVA, $P<0.05$), we fit their normalized response tuning curves to grating drifting angle θ with a bimodal Gaussian function[56]

$$R(\theta)=R_{offset}+R_{pref}e^{-\frac{ang(\theta-\theta_{pref})^2}{2\sigma^2}}+R_{oppo}e^{-\frac{ang(\theta-\theta_{pref}+180)^2}{2\sigma^2}}$$

Here θ_{pref} is the preferred orientation, R_{offset} is a constant offset, and R_{pref} and R_{oppo} are the responses at θ_{pref} and $\theta_{pref}-180$ degrees, respectively. $ang(x)=\min(x, x-360, x+360)$ wraps angular values onto the interval 0° to 180°. For the dLGN data, only ROIs whose tuning curves were well fit by the bimodal Gaussian function were considered orientation selective. In LP and LM data, ROIs were considered visually responsive if a two-sided t test between the fluorescence values during the baseline and stimulus period resulted in significance at an alpha value of 0.001.

For determining the frame-to-frame correlations, we calculated the 2-D correlation between frames of registered image stacks using the Matlab function corr2. The brightness of imaged varicosities from the dLGN thalamocortical projections was determined by normalizing pixel fluorescence value to the square of the excitation laser intensity[57]. Contrast was then determined by taking profiles across axonal structures and normalizing these profiles to the peak intensity.

Statistical methods. All statistical analyses were performed in Matlab (MathWorks) or Prism (GraphPad). We used parametric and nonparametric ANOVA, Wilcoxon's rank-sum tests, and Kolmogorov–Smirnov test. All tests were two-tailed. Error bars are s.e.m. or s.d., as indicated in figure legends and main text. No statistical methods were used to predetermine sample size. However, sample sizes are consistent with those reported in previous publications[31,55]. Data collection was randomized in the organization of the experimental conditions and visual stimulus presentations. Data collection and analysis were not performed blind to the condition of the experiments. Data distribution was assumed to be normal, but this was not formally tested. No animals and no data points were excluded from the analyses.

Reporting Summary. Further information on experimental design is available in the Nature Research Reporting Summary linked to this article.

Data, reagent and code availability. The data that support the findings of this study are presented in the paper and the supplementary materials and all raw

imaging data are available upon request. All routine analysis methods are included in the Methods section, and Matlab codes are deposited in GitHub (https://github.com/gerardj-broussard/BroussardEtAl2018.git). Plasmids encoding axon-GCaMP and bicistronic variants (accession numbers: MH282423, MH282424, MH282425, MH282426, MH282427, MH282429, MH282430, MH282432) have been made available in the Addgene plasmid repository (plasmid numbers 111261–112010).

References

51. Kim, J. H. et al. High cleavage efficiency of a 2A peptide derived from porcine teschovirus-1 in human cell lines, zebrafish and mice. *PLoS One* **6**, e18556 (2011).
52. Kang, M., Day, C. A., Kenworthy, A. K. & DiBenedetto, E. Simplified equation to extract diffusion coefficients from confocal FRAP data. *Traffic* **13**, 1589–1600 (2012).
53. Pologruto, T. A., Sabatini, B. L. & Svoboda, K. ScanImage: flexible software for operating laser scanning microscopes. *Biomed. Eng. Online* **2**, 13 (2003).
54. Kalatsky, V. A. & Stryker, M. P. New paradigm for optical imaging: temporally encoded maps of intrinsic signal. *Neuron* **38**, 529–545 (2003).
55. Marshel, J. H., Garrett, M. E., Nauhaus, I. & Callaway, E. M. Functional specialization of seven mouse visual cortical areas. *Neuron* **72**, 1040–1054 (2011).
56. Anderson, J. S., Carandini, M. & Ferster, D. Orientation tuning of input conductance, excitation, and inhibition in cat primary visual cortex. *J. Neurophysiol.* **84**, 909–926 (2000).
57. Theer, P. & Denk, W. On the fundamental imaging-depth limit in two-photon microscopy. *J. Opt. Soc. Am. A Opt. Image Sci. Vis.* **23**, 3139–3149 (2006).

nature research

Corresponding author(s): Lin Tian, Leopoldo Petreanu

Reporting Summary

Nature Research wishes to improve the reproducibility of the work that we publish. This form provides structure for consistency and transparency in reporting. For further information on Nature Research policies, see Authors & Referees and the Editorial Policy Checklist.

Statistical parameters

When statistical analyses are reported, confirm that the following items are present in the relevant location (e.g. figure legend, table legend, main text, or Methods section).

n/a	Confirmed	
☐	☒	The exact sample size (*n*) for each experimental group/condition, given as a discrete number and unit of measurement
☐	☒	An indication of whether measurements were taken from distinct samples or whether the same sample was measured repeatedly
☐	☒	The statistical test(s) used AND whether they are one- or two-sided *Only common tests should be described solely by name; describe more complex techniques in the Methods section.*
☐	☒	A description of all covariates tested
☐	☒	A description of any assumptions or corrections, such as tests of normality and adjustment for multiple comparisons
☐	☒	A full description of the statistics including central tendency (e.g. means) or other basic estimates (e.g. regression coefficient) AND variation (e.g. standard deviation) or associated estimates of uncertainty (e.g. confidence intervals)
☐	☒	For null hypothesis testing, the test statistic (e.g. *F*, *t*, *r*) with confidence intervals, effect sizes, degrees of freedom and *P* value noted *Give P values as exact values whenever suitable.*
☒	☐	For Bayesian analysis, information on the choice of priors and Markov chain Monte Carlo settings
☒	☐	For hierarchical and complex designs, identification of the appropriate level for tests and full reporting of outcomes
☒	☐	Estimates of effect sizes (e.g. Cohen's *d*, Pearson's *r*), indicating how they were calculated
☐	☒	Clearly defined error bars *State explicitly what error bars represent (e.g. SD, SE, CI)*

Our web collection on statistics for biologists may be useful.

Software and code

Policy information about availability of computer code

Data collection	ScanImage software in a Matlab environment and Zeiss Zen software were used for data collection.
Data analysis	Matlab and PRISM software were used for all data processing and statistical analyses. All Matlab code is deposited in Github and also available upon request.

For manuscripts utilizing custom algorithms or software that are central to the research but not yet described in published literature, software must be made available to editors/reviewers upon request. We strongly encourage code deposition in a community repository (e.g. GitHub). See the Nature Research guidelines for submitting code & software for further information.

Data

Policy information about availability of data

All manuscripts must include a data availability statement. This statement should provide the following information, where applicable:

- Accession codes, unique identifiers, or web links for publicly available datasets
- A list of figures that have associated raw data
- A description of any restrictions on data availability

The data that support the findings of this study are presented in the paper and the supplementary materials and all raw imaging data are available upon request. All routine analysis methods are included in the Methods section and MATLAB codes are deposited in github (https://github.com/gerardj-broussard/

BroussardEtAl2018.git). Plasmids encoding axon-GCaMP and bicistronic variants (Accession numbers: MH282423, MH282424, MH282425, MH282426, MH282427, MH282429, MH282430, MH282432) have been made available in the Addgene plasmid repository (plasmid number 111261-112010).

Field-specific reporting

Please select the best fit for your research. If you are not sure, read the appropriate sections before making your selection.

☒ Life sciences ☐ Behavioural & social sciences ☐ Ecological, evolutionary & environmental sciences

For a reference copy of the document with all sections, see nature.com/authors/policies/ReportingSummary-flat.pdf

Life sciences study design

All studies must disclose on these points even when the disclosure is negative.

Sample size	No statistical methods were used to predetermine sample size. However, sample sizes are consistent with those reported in previous publications (12,13).
Data exclusions	No data were excluded from this study
Replication	Each experiment was performed on multiple cultures or animal subjects. All attempts were successful.
Randomization	Animals and cultures were randomly assigned for transduction with the different constructs described in the manuscript.
Blinding	Blinding was not used in this study. The extreme differences in the expression patterns of targeted and non-targeted constructs made it immediately apparent which construct was transduced in each subject/culture.

Reporting for specific materials, systems and methods

Materials & experimental systems

n/a	Involved in the study
☒	☐ Unique biological materials
☒	☐ Antibodies
☒	☐ Eukaryotic cell lines
☒	☐ Palaeontology
☐	☒ Animals and other organisms
☒	☐ Human research participants

Methods

n/a	Involved in the study
☒	☐ ChIP-seq
☒	☐ Flow cytometry
☒	☐ MRI-based neuroimaging

Animals and other organisms

Policy information about studies involving animals; ARRIVE guidelines recommended for reporting animal research

Laboratory animals	For derivation of primary neuronal cultures, P0 or E18 Sprague Dawley pups were used. For in vivo imaging and histological experiments, C57Bl6, Scnn1a-Tg3-Cre, Rbp4-Cre and Ntsr1-Cre mice between the ages of 8 and 30 weeks of age with weights ranging from 19g-27g were used. Use of male and female animals was matched between tests of the two constructs.
Wild animals	The study did not involve wild animals.
Field-collected samples	The study did not involve in field-collected samples.